ENHANCING OXYGEN TRANSPORT THROUGH MIXED-IONIC-AND-ELECTRONIC-CONDUCTING CERAMIC MEMBRANES

Anthony S. Yu

A DISSERTATION

in

Chemical and Biomolecular Engineering

Presented to the Faculties of the University of Pennsylvania

in Partial Fulfillment of the Requirements for the

Degree of Doctor of Philosophy

2015

PREVIEW

Supervisor of Dissertation

_____

Raymond J. Gorte, Professor, CBE

Co-Supervisor of Dissertation

_____

John M. Vohs, Professor, CBE

Graduate Group Chairperson

_____

Raymond J. Gorte, Professor, Chemical and Biomolecular Engineering

Dissertation Committee

Daeyeon Lee, Associate Professor, Chemical and Biomolecular Engineering

Peter K. Davies, Professor, Material Science and Engineering

ProQuest Number: 3720914

All rights reserved

INFORMATION TO ALL USERS
The quality of this reproduction is dependent upon the quality of the copy submitted.

In the unlikely event that the author did not send a complete manuscript
and there are missing pages, these will be noted. Also, if material had to be removed,
a note will indicate the deletion.



ProQuest 3720914

Published by ProQuest LLC (2015). Copyright of the Dissertation is held by the Author.

All rights reserved.
This work is protected against unauthorized copying under Title 17, United States Code
Microform Edition © ProQuest LLC.

ProQuest LLC.
789 East Eisenhower Parkway
P.O. Box 1346
Ann Arbor, MI 48106 - 1346

PREVIEW

This work is dedicated to my family

PREVIEW

Acknowledgements

I would first like to thank my advisors Professors Raymond Gorte and John Vohs for their guidance and advice throughout my studies. Through our daily discussions in lab I have learned from them everything I know about conducting scientific research, and how to think like an engineer. Thank you both for being great advisors.

I would also like to thank my past and present lab mates, especially Lawrence and Taesik who were always willing to give useful suggestions and encouragement when research was going slow.

My life at Penn would not have been half as enjoyable without the many friends that I have made during my time here. Thank you all for the great memories; you guys are awesome! A special thank you to Elva, whose continuous support and care has gotten me through all the struggles and frustrations I have faced during my time at Penn.

Last but not least, my deepest gratitude to my parents as well as my siblings Amy and Tim. Moving away from home to the U.S. has not always been easy, and I could not have done it without their unconditional love and support.

PREVIEW

ABSTRACT

ENHANCING OXYGEN TRANSPORT THROUGH MIXED-IONIC-AND-ELECTRONIC-CONDUCTING CERAMIC MEMBRANES

Anthony S. Yu

Raymond J. Gorte

John M. Vohs

PREVIEW

Ceramic membranes based on Mixed-Ionic-and-Electronic-Conducting (MIEC) oxides are capable of separating oxygen from air in the presence of an oxygen partial-pressure gradient. These MIEC membranes show great promise for oxygen consuming industrial processes, such as the production of syngas from steam reforming of natural gas (SRM), as well as for electricity generation in Solid Oxide Fuel Cells (SOFC). For both applications, the overall performance is dictated by the rate of oxygen transport across the membrane. Oxygen transport across MIEC membranes is composed of a bulk oxygen-ion diffusion process and surface processes, such as surface reactions and adsorption/desorption of gaseous reactants/products. The main goal of this thesis was to determine which process is rate-limiting in order to significantly enhance the overall rate of oxygen transport in MIEC membrane systems.

The rate-limiting step was determined by evaluating the total resistance to oxygen transfer, R_{tot}. R_{tot} is the sum of a bulk diffusion resistance in the membrane itself, R_b, and

interfacial loss components, R_s. R_b is a function of the membrane's ionic conductivity and thickness, while R_s arises primarily from slow surface-exchange kinetics that cause the $P(O_2)$ at the surfaces of the membrane to differ from the $P(O_2)$ in the adjacent gas phases. R_{tot} can be calculated from the Nernst potential across the membrane and the measured oxygen flux. The rate-limiting process can be determined by evaluating the relative contributions of the various losses, R_s and R_b, to R_{tot}. Using this method, this thesis demonstrates that for most membrane systems, R_s is the dominating factor.

In the development of membrane systems with high oxygen transport rates, thin membranes with high ionic conductivities are required to achieve fast bulk oxygen-ion diffusion. However, as membrane thickness is decreased, surface reaction kinetics become more important in determining the overall transport rate. The two approaches to increase surface reaction kinetics and decrease R_s that were examined in this thesis involved modifying the surface microstructure, as well as adding both metallic (e.g. Pt) and oxide (e.g. CeO_2, $La_{0.8}Sr_{0.2}FeO_3$) catalysts to both membrane surfaces. These two approaches were investigated for single-phase MIEC membrane reactors ($La_{0.9}Ca_{0.1}FeO_{3-\delta}$), as well as composite membrane reactors composed of an electronic conductor ($La_{0.8}Sr_{0.2}CrO_{3-\delta}$) and an ionic conductor (YSZ).

The use of catalysts and microstructure modifications to decrease interfacial losses is equally important for SOFCs. In this thesis, the electrochemical activity and microstructure of metallic catalysts formed by "ex-solving" metals from an oxide lattice, and oxide catalysts deposited by Atomic Layer Deposition (ALD) were investigated. It is shown that these methods for depositing catalysts resulted in very different effects on electrode performance when compared to the same catalysts deposited by wet

PREVIEW

impregnation. For example, when transition metals, such as Ni and Co, were "ex-solved" from a $La_{0.8}Sr_{0.2}CrO_{3-\delta}$ anode lattice, these "ex-solved" metal particles not only exhibited great catalytic activity, they were also less prone to coking compared to their wet impregnated counterparts. On the cathode side, thin layers of various oxides (e.g. Al_2O_3, CeO_x, SrO) that were deposited using ALD also exhibited drastically different electrochemical activity compared to their wet impregnated counterparts. It was determined that differences in electrochemical activity could be attributed to a difference in the oxide morphology, showing that a catalyst's microstructure and morphology are very important in dictating its overall activity in SOFC electrodes.

PREVIEW

Table of Contents

Chapter 1. Introduction 1

1.1 Motivation 1

1.2 Operating Principles 3

1.2.1 Ceramic Membrane Reactors 3

1.2.2 Solid Oxide Fuel Cells 5

1.3 State-of-the-Art Materials 7

1.3.1 MIEC Oxides for Membrane Reactors for Syngas Production 8

1.3.1.1 Single Phase Materials 8

1.3.1.2 Dual Phase Composite Materials 10

1.3.2 Materials for Solid Oxide Fuel Cells 12

1.3.2.1 Electrolyte Materials 12

1.3.2.2 Anode Materials 13

1.3.2.3 Cathode Materials 15

1.4 Determining the Rate-Limiting Step for Oxygen Transport 16

1.5 Enhancing Membrane Performance 19

1.5.1 Increasing the Rate of Bulk Diffusion of Oxygen Ions 19

1.5.2 Increasing the Rate of Surface Processes 20

1.6 References 22

PREVIEW

Chapter 2. Decreasing Interfacial Losses with Catalysts in $La_{0.9}Ca_{0.1}FeO_{3-\delta}$ Membrane Reactors for Syngas Production 33

2.1 Introduction 33

2.2 Experimental 37

2.3 Results 39

2.3.1 Membrane Characterization and Oxygen Permeation Flux 39

2.3.2 Evaluating the Contributions of R_b and R_s to R_{tot} 45

2.3.3 Relative Importance of Air- and Fuel-Side Catalysts 49

2.4 Discussion 55

2.5 Conclusions 57

2.6 References 58

Chapter 3. Surface Modifications of $La_{0.8}Sr_{0.2}CrO_{3-\delta}$-YSZ Dual-Phase Membranes for Syngas Production 67

3.1 Introduction 67

3.2 Experimental 70

3.3 Results 74

3.3.1 Physical Characterization of LSCr-YSZ Composites 74

3.3.2 Oxygen Permeation Fluxes 77

3.3.3 Effect of Surface Structure 82

3.4 Discussion 86

3.5 Conclusions 88

3.6 References 88

PREVIEW

Chapter 4. Infiltrated $La_{0.8}Sr_{0.2}CrO_{3-\delta}$ Anodes for Solid Oxide Fuel Cells: Structural and Catalytic Aspects 92

4.1 Introduction 92

4.2 Experimental 96

4.3 Results and Discussion 99

4.3.1 Characterization of LSCr Samples 99

4.3.2 Comparison of LSCr and LSCM 100

4.3.3 Doping LSCr with Catalytic Transition Metals 107

4.4 Conclusions 112

4.5 References 113

Chapter 5. An Investigation of Oxygen Reduction Kinetics in $La_{0.8}Sr_{0.2}FeO_{3-\delta}$ Electrodes 117

5.1 Introduction 117

5.2 Experimental 122

5.3 Results 128

5.3.1 Effect of Calcination Temperature on LSF-YSZ Composite 128

5.3.2 $P(O_2)$ Dependence of LSF-YSZ Electrodes 131

5.3.3 Inert Al_2O_3 Blocking Layers 137

5.4 Discussion 142

5.5 Conclusions 148

5.6 References 149

PREVIEW

Chapter 6. Modification of SOFC Cathodes by Atomic Layer Deposition 156

6.1 Introduction 157

6.2 Experimental 161

6.3 Results 165

6.3.1 ALD Films of CeO_x on LSF-YSZ 166

6.3.2 ALD Films of SrO on LSF-YSZ 171

6.3.3 ALD Films of CeO_x on LSCo-YSZ and BSCF-YSZ 177

6.4 Discussion 179

6.5 Conclusions 182

6.6 References 183

6.7 Supplemental Information 192

6.7.1 ALD System Setup 192

6.7.2 Characterization of Ce ALD 193

Chapter 7. Conclusions 195

PREVIEW

List of Tables

Table 2.1	Catalyst composition and membrane thickness of LCF membranes	38
Table 2.2	R_{tot} with and without catalyst	43
Table 2.3	Activation energies for oxygen permeation of LCF membranes	54
Table 3.1	LSCr-YSZ membrane Compositions	73
Table 3.2	Total Resistances of LSCr-YSZ Membranes M1, M5, and M6	86
Table 4.1	Carbon deposition comparison on various oxides	111
Table 6.1	Comparison of the change in unoccupied surface oxygen vacancies after CeO_2 ALD with that for Al_2O_3 ALD.	170
Table 6.2	Oxygen vacancies per unit cell at $P(O_2)$ = 0.2 bar, 873K and 973K for $La_{0.8}Sr_{0.2}FeO_{3-\delta}$ (LSF), $La_{0.6}Sr_{0.4}CoO_{3-\delta}$ (LSCo), and $Ba_{0.5}Sr_{0.5}Co_{0.8}Fe_{0.2}O_{3-\delta}$ (BSCF).	179

PREVIEW

List of Figures

Figure 1.1	Operating principles for oxygen transport in ceramic membranes	5
Figure 1.2	Operating principles for SOFC	6
Figure 1.3	Idealized schematic of a two-phase, MIEC conductor. The dark and light crystallites symbolize the electronic and ionic conducting phases.	11
Figure 1.4	Schematics showing the $P(O_2)$ profile (dotted line) across the membrane in an ideal case where the rate of reactions are infinitely fast, compared to that for a real system. R_s arises from the loss in driving force for oxygen transport due to slow surface reaction kinetics that cause a reduction in $\Delta P(O_2)$ across the membrane.	18
Figure 2.1	X-Ray diffraction patterns of the dense LCF layer after calcination at 1673 K, and after reduction at 1173 K in CO for 4 hours.	40
Figure 2.2	SEM Micrographs showing the porous-dense-porous microstructure of the calcined LCF membrane. Inset showing the dense layer was taken from the native surface.	41
Figure 2.3	Temperature dependence of the oxygen permeation flux of an unmodified LCF membrane (M1) (during heating (◆) and cooling (◇)), and that of a LCF membrane with 1 wt% Pt and 5 wt% CeO_2 on the fuel-side and 5 wt% LSF on the air-side (M6) (during heating (●) and cooling (○)).	42
Figure 2.4	SEM Micrographs showing the microstructure change of the fuel-side porous layer before (a) and after (b) oxygen permeation measurements. Insets show higher magnification of the porous layer surface.	45
Figure 2.5	Comparison of the oxygen flux of LCF membranes with 75 µm (M6) (●), 260 µm (M7) (▲), and 350 µm (M8) (■) dense layers. All membranes had 1 wt% Pt and 5 wt% CeO_2 catalysts on the fuel-side, and 5 wt% LSF catalyst on the air-side.	47
Figure 2.6	Dependence of R_{tot} on the membrane thickness at 973 K (●) and 1073 K (■). Dotted lines are linear fit lines extrapolating to zero membrane thickness to estimate R_s.	48

PREVIEW

Figure 2.7	Temperature dependence of the oxygen flux of LCF membranes with (M5) (▲) and without (M1) (◆) addition of 5 wt% LSF on the air-side. The oxygen flux can be further enhanced with addition of 1 wt% Pt and 5 wt% CeO_2 to the fuel-side (M6) (●).	51
Figure 2.8	Temperature dependence of the oxygen flux of LCF membranes with addition of various catalysts on the fuel-side; unmodified (M1) (◆), 1 wt% Pt (M2) (■), 5 wt% CeO_2 (M3) (▲), and 1 wt% Pt with 5 wt% CeO_2 (M4)(●).	53
Figure 2.9	Arrhenius Plot showing the difference in activation energy for oxygen transport after addition of catalysts on the fuel side; unmodified (◆), 1 wt% Pt (■), 5 wt% CeO_2 (▲), and 1 wt% Pt with 5 wt% CeO_2 (●).	54
Figure 3.1	XRD pattern of a dense LSCr(◆)-YSZ(▲) dual phase membrane.	75
Figure 3.2	Temperature dependence of the total conductivity of a dense LSCr-YSZ slab measured while heating (●) and cooling (○).	75
Figure 3.3	SEM image of LSCr-YSZ membrane showing the porous-dense-porous structure with insets showing higher magnification of the dense and porous layers.	77
Figure 3.4	Temperature dependence of the oxygen permeation flux of LSCr-YSZ membranes with LSCr-YSZ composite porous layer and various catalysts on the syngas side: unmodified (M1) (●), 5 wt% CeO_2 (M2) (■), and 5 wt% CeO_2 with 1 wt% Pt (M3)(▲).	78
Figure 3.5	R_{tot} of 115 μm and 650 μm thick LSCr-YSZ composite membranes at 973 K (▲) and 1073 K (■). The slopes of the linear fits are the corresponding ionic conductivities at those temperatures.	81
Figure 3.6	Cartoon showing the different surface microstructures for the syngas side porous layers in membrane M1 and M5 with YSZ (light region) and LSCr (dark region). Membrane M1 has a porous layer with a random mixture of LSCr-YSZ, while membrane M5 has a porous layer with LSCr infiltrated on top of YSZ. The dense layers in both membranes are LSCr-YSZ composite.	83
Figure 3.7	Temperature dependence of the oxygen permeation flux of a membrane with an LSCr-YSZ composite porous layer on the syngas side (M1) (●), in comparison with that of a membrane with a pure YSZ porous layer on the syngas side infiltrated with LSCr (M5) (▲). Addition of Pt to M5 further improves oxygen flux	84

PREVIEW

(M6).

Figure 4.1	XRD patterns of (a) YSZ-LSCr powder mixture before reduction, (b) YSZ-LSCr powder mixture after reduction (800˚C, 4h in dry H_2), and (c) measurement-ready LSCr (45 wt%) infiltrated anode with ceria (5 wt%). "x" marks show ceria peak positions, and vertical shaded bands denote YSZ peaks. Diamond marks show an unknown peak at 43˚.	100
Figure 4.2	Electrical conductivity of the 45 wt% perovskite-YSZ composite in humidified H_2 (3 % H_2O) as a function of temperature.	102
Figure 4.3	V-i and V-power density polarization curves for cells with 45 wt% perovskite calcined at 1473 K, with 5 wt% ceria and 0.5 wt% Pd. Fuel condition: 973 K in humidified H_2 (3 % H_2O). Cathodes were exposed to stagnant, ambient air. The thin and thick lines correspond to the voltage and power curves, respectively.	103
Figure 4.4	SEM images of a YSZ porous scaffold infiltrated with either LSCr or LSCM. (a) LSCr before reduction, (b) LSCr after reduction, (c) LSCM before reduction, and (d) LSCM after reduction. The scale bars are for 1μm.	105
Figure 4.5	Open circuit Cole-Cole plots for cells with 45 wt% LSCr calcined at 1473 K and (open circles) 0.5 wt% Pd or (closed circles) 0.5 wt% Pd plus 5 wt% CeO_2 added to enhance catalytic activity. Operating conditions: 973 K in humidified H_2 (3 % H_2O). Cathodes were exposed to stagnant, ambient air.	106
Figure 4.6	V-i and V-power density curves for cells with 45 wt% transition-metal doped LSCr calcined at 1473 K. The transition metal dopants are indicated in the figure. Operating conditions: 973 K in humidified H_2 (3 % H_2O). Cathodes were exposed to stagnant, ambient air. Open and closed symbols correspond to the voltage and power curves, respectively.	109
Figure 4.7	Open circuit voltage Cole-Cole plots for cells with 45 wt% transition-metal doped LSCr calcined at 1473 K. The transition metal dopants are indicated in the figure. For one cell undoped LSCr was used a Pd (0.5 wt%) catalyst was added by infiltration. Operating conditions: 973 K in humidified H_2 (3 % H_2O). Cathodes were exposed to stagnant, ambient air.	110
Figure 5.1	Schematic showing the steps involved in ALD	121

PREVIEW

Figure 5.2	NO_2 flow titration results on a) empty reactor, b) pure LSF, and c) the same LSF sample coated with 20 cycles of Al_2O_3. The titration was carried out at 473 K. NO_2 reacts with the LSF surface, which results in a lag between the onset of the NO_2 (m/z = 46) signal compared to the NO signal (m/z = 30). Due to the low intensity of the m/z = 46 signal, a 10-point average fit (black line) has been overlaid on the raw data (grey squares).	126
Figure 5.3	Surface fraction of uncoated LSF as determined by NO_2 flow titration experiments, plotted as a function of the number of Al_2O_3 ALD cycles (closed symbols). The dashed line is an empirical fit to the experimental data assuming the growth proceeds via the random deposition model[35] with a per-cycle coverage of 6%. The open symbol corresponds to an Al_2O_3-coated LSF sample treated to 1073 K for 4 hours before the experiment.	127
Figure 5.4	SEM images of LSF-YSZ electrodes prepared by infiltration after calcination to (a) 1123 K and (b) 1373 K.	129
Figure 5.5	Nyquist plots of LSF-YSZ cathode symmetric cells measured at 973 K, under open circuit conditions in pure oxygen, measured as a function of LSF calcination temperature: 1123 K (closed symbols) and 1373 K (open symbols).	131
Figure 5.6	Nyquist plots of LSF-YSZ cathode symmetric cells measured at 973 K and open circuit conditions as a function of oxygen partial pressure: (a) LSF-YSZ calcined to 1123 K, (b) LSF-YSZ calcined to 1373 K. The impedance spectra have been offset for clarity. The spectra in (a) were measured at the same $P(O_2)$ as in (b).	132
Figure 5.7	Oxygen partial pressure dependence of processes in the impedance spectra of LSF-YSZ electrodes at 973 K: (•) total polarization resistance of a cell heated to 1123 K, (o) high-frequency (HF) polarization resistance of a cell heated to 1373 K, and (◊) low-frequency (LF) polarization resistance of a cell heated to 1373 K.	134
Figure 5.8	Nyquist plots of LSF-YSZ cathode symmetric cells measured at 973 K in 5% O_2 in argon as a function of applied current density: (a) LSF-YSZ calcined to 1123 K, (b) LSF-YSZ calcined to 1373 K.	136
Figure 5.9	Nyquist plots of LSF-YSZ cathode symmetric cells calcined to 1123 K and measured at 873 K before and after ALD treatment. The impedance spectra have been offset for clarity.	139
Figure 5.10	Nyquist plots of LSF-YSZ cathode symmetric cells calcined to 1123 K tested at 973 K before and after a 5-cycle Al_2O_3 ALD. Performance is partly restored after the ALD layer disintegrates at	140

PREVIEW

1073 K.

Figure 5.11	Electrode polarization resistance for an LSF-YSZ symmetric cell, calcined to 1123 K and coated with 50 ALD cycles of Al_2O_3, measured under open circuit conditions (white regions) at 873 K as a function of current load (the load was applied immediately before the measurements (grey regions)).	141
Figure 5.12	The polarization resistance, R_p, of LSF-YSZ cathodes heated to 1123 K and coated with a thin coating of alumina as a function of the available LSF surface fraction, as determined by NO_2 flow titration experiments (open symbols). The relationship between LSF-YSZ electrode surface area and R_p from Reference 7 is given on the other two axes (closed symbols). The electrode with a surface area of 1.45 m^2/g was identical to LSF-YSZ electrodes used in this study and was also calcined to 1123 K. All data were acquired at 873 K under no current load.	144
Figure 5.13	Sticking coefficient, *S*, plotted as a function of the availability of the LSF surface (as determined from flow titration experiments).	147
Figure 6.1	Amounts of Ce (■), Sr (●), or Al (▲)[31] deposited per ALD cycle as measured gravimetrically.	165
Figure 6.2	Nyquist plots of LSF-YSZ cathode symmetric cells calcined to 1123 K and measured at a) 873K and b) 973K before and after CeO_x ALD treatment. The impedance spectra have been offset for clarity.	168
Figure 6.3	Nyquist plots comparing the performance of an LSF-YSZ cathode symmetric cell calcined to 1123 K and tested at 973 K before and after 5 cycles CeO_x ALD. Performance of the cell was partially restored after calcination at 1073 K for 1 hour.	171
Figure 6.4	Nyquist plots of LSF-YSZ cathode symmetric cells calcined to 1123 K and measured at a) 873 K and b) 973 K before and after SrO ALD treatment. The impedance spectra have been offset for clarity.	173
Figure 6.5	Coverage dependence of LSF-YSZ symmetric cell electrode resistance at 973 K after ALD of CeO_x, SrO, or Al_2O_3. Dashed line is a linear fit to the Al_2O_3 and SrO data.	174
Figure 6.6	Comparison of the effect of applying current on LSF-YSZ symmetric cells treated with 5 cycles of a) CeO_x vs. 5 cycles of b) SrO ALD. Initial performance at open circuit is shown in open symbols, while the performance at open circuit after polarization at	176

PREVIEW

400 mA cm^{-2} for 2 minutes is shown in closed symbols.

Figure 6.7	Electrode resistances as a function the number of CeO_x ALD cycles for cathode symmetric cells composed of LSF-YSZ calcined to 1123K (●), LSCo-YSZ calcined to 973K (△), and BSCF-YSZ calcined to 973K (■) at operating temperatures of a) 873K, and b) 973K. The dashed lines are meant to guide the eye.	178
Figure S.1	Schematic of home built ALD system. The temperature of the sample chamber was controlled with a furnace, while the rest of the system was wrapped in heating tape. The position of the pressure sensor and thermocouples are noted in the schematic.	192
Figure S.2	Temperature programmed oxidation of LSF wafers with $Ce(DMP)_4$ deposited at various sample chamber temperatures (T_{ALD}).	194

PREVIEW

Chapter 1. Introduction*

1.1 Motivation

Rising concerns in the world today regarding increased energy consumption and demand has motivated the development of more energy efficient alternatives to conventional industrial processes for the production of valuable chemicals and power generation. Among the emerging technologies that show great promise in this area are those involving the use of ceramic membranes based on Mixed-Ionic-and-Electronic-Conductors (MIEC). These types of ceramic membranes are able to passively separate oxygen from ambient air at temperatures above 700ºC, which in turn provides an efficient method to supply pure oxygen for oxidation reactions. One industrial process where incorporation of MIEC ceramic membranes could be potentially game changing is the steam reforming of methane to produce syngas. The production of syngas (a mixture of H_2, CO, and CO_2) is one of the most important processes in the chemical industry[1] since it is a key first step in the production of H_2, ammonia, and methanol, along with all the chemicals and materials that are made from these basic building blocks. The primary feedstock for producing syngas is natural gas, with methane as the main component. In most large-scale processes, the methane is oxidized by steam (Steam Reforming of Methane, SRM) to yield the desired products according to Equation 1.1:

$$CH_4 + H_2O \rightarrow CO\ (CO_2) + H_2 \qquad 1.1$$

*Several sections of this chapter were published as a review paper in Energy and Environmental Science, 7 (2014) 944-953. Copyright: 2014, The Royal Society of Chemistry.

PREVIEW

SRM is highly endothermic, requiring the addition of large amounts of heat both to maintain the reaction temperature and to favor high equilibrium conversions. A typical temperature range for the reactor exit in the primary reforming reactor is 850 to 900°C, which is required in order to achieve equilibrium CH_4 conversions above 90% at the pressures used in industrial scale reactors.[1] The addition of heat at these high temperatures is challenging and expensive; and, unlike the case for mildly endothermic reactions, such as reforming of higher hydrocarbons to produce olefins and aromatics, it is not possible to use staged reactors with intermediate heat exchange. In conventional SRM, heating is accomplished through a highly energy intensive process where tubular reactors are heated in a large furnace by burning a source of fuel.[1] Alternatively, temperatures can also be maintained by adding O_2 to the feed in a process referred to as Auto-Thermal Reforming (ATR). With ATR, heat for the reforming reaction is provided by using a small part of the feed with the added O_2 in a highly exothermic combustion reaction. Having a pure source of oxygen is critical in ATR to avoid diluting the produced syngas with nitrogen. Pure oxygen is conventionally produced by cryogenically distilling liquefied air, which is an energy intensive process in itself. Significant improvement in the energy efficiency of syngas production can be achieved by producing pure oxygen and delivering it to the reaction through the use of high-temperature ceramic membrane reactors.[2]

In addition to O_2 consuming industrial processes, MIEC membranes could also be a potentially disruptive technology in power generation. MIEC ceramic membranes can be configured and utilized as Solid Oxide Fuel Cells (SOFC), which are electrochemical devices capable of converting chemical energy directly to electrical energy. In SOFC, the

PREVIEW

oxygen transported across the membrane is used to oxidize a fuel source in an electrochemical reaction that produces electrons. Unlike in conventional thermal power plants where heat generated by burning fuel is converted into mechanical energy, which is subsequently converted to electrical energy, the electrochemical reactions that occur in a SOFC are not constrained by the Carnot efficiency. As a result, SOFC can be significantly more efficient than combustion based power generation. Furthermore, additional energy can be recovered from the waste heat generated by the oxidation reactions in SOFC by incorporating a steam turbine cycle. The overall efficiency of a combined heat and power generation system can reach as high as 80%.[3-5] In the following sections, the operating principles and basic components for ceramic membrane reactors and SOFC will be discussed.

PREVIEW

1.2 Operating principles

1.2.1 Ceramic Membrane Reactors

A membrane reactor is composed of a dense MIEC oxide membrane that can transport oxygen across the membrane by converting gaseous O_2 into O^{2-} ions. The basic operating principles for these ceramic membrane reactors are shown schematically in Figure 1.1. Gas-phase O_2 reacts at one surface of the membrane to form oxygen ions that then migrate through the oxide lattice, with counter migration of electrons to balance the charge. The oxygen ions can either recombine to give a pure stream of oxygen on the permeate side, or the ions can be utilized to oxidize a fuel mixture on the reforming fuel

side. The driving force for oxygen migration is the $P(O_2)$ difference across the membrane. In the case of oxygen separation, the air on the feed side is often pressurized to create the $P(O_2)$ difference. If used to run an oxidation reaction, the driving force is the $P(O_2)$ difference between air and the gas on the fuel side, with the $P(O_2)$ on the fuel side being established by equilibrium with the fuel-oxidation reactions. For example, with H_2 oxidation, the equilibrium $P(O_2)$ would be established by the $P(H_2O)$:$P(H_2)$ ratio. Using the fact that the diffusion of oxygen ions in the membrane will be proportional to the gradient in the chemical potential of O_2, one can derive that the O_2 flux across the membrane will be given by Equation 1.2:

$$J_{O_2} = \frac{R_g T \sigma_{amb}}{16 F^2 \lambda} \ln\left(\frac{PO_{2,air}}{PO_{2,syngas}}\right) \qquad 1.2$$

In this equation, J_{O2} is the O_2 flux, R_g is the gas constant, F is Faraday's constant, and λ is the thickness of the membrane. The ambipolar conductivity, σ_{amb}, is related to the electronic (σ_{el}) and ionic (σ_i) conductivities of the membrane material according Equation 1.3.

$$\sigma_{amb} = \left(\frac{\sigma_i \sigma_{el}}{\sigma_i + \sigma_{el}}\right) \qquad 1.3$$

A primary assumption used in the derivation of Equation 1.2 is that equilibrium is established between the surfaces of the membrane and the gas phase on each side. One of the main conclusions of this thesis is the demonstration that this assumption of equilibrium at the interface is often a poor one, and that special measures must be taken to bring the surfaces back into equilibrium with its adjacent gas phase.

PREVIEW

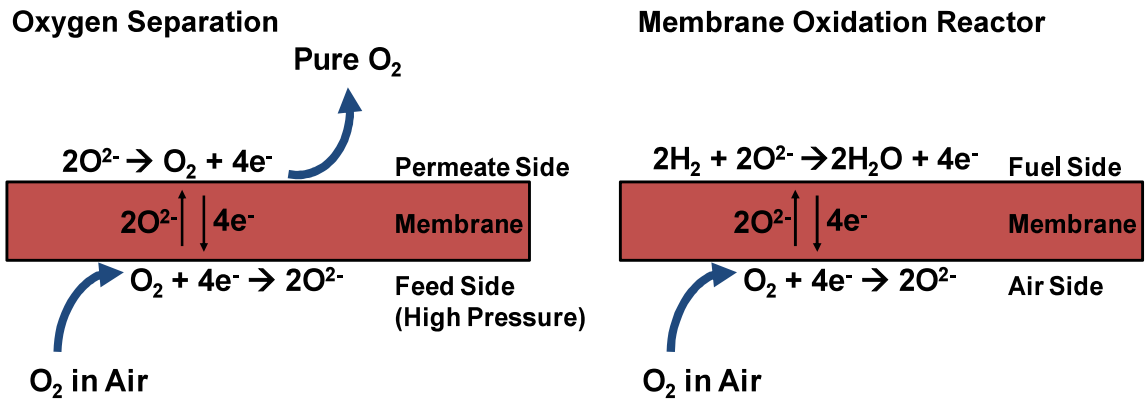


Figure 1.1: Operating principles for oxygen transport in ceramic membranes

PREVIEW

1.2.2 Solid Oxide Fuel Cells

A SOFC is an electrochemical device that can convert chemical energy directly into electricity through an oxidation reaction with a source of fuel. SOFC are composed of three ceramic layers: a porous anode that facilitates the oxidation of fuel, a porous cathode that catalyzes the reduction of gaseous oxygen to form O^{2-} ions, and a dense electrolyte in between the two electrodes that transports the oxygen anions from the cathode to the anode. As shown in Figure 1.2, the operating principles for SOFC are very similar to that of membrane reactors, with the main difference being that the electrolyte layer in SOFC should ideally be a dense ceramic with purely ionic conductivity and no electronic conductivity. This allows the electrons produced in the fuel oxidation reaction to be run through an external circuit to do work. During operation, gas-phase oxygen is electrochemically reduced to O^{2-} ions by electrons as shown in Equation 1.4:

$$O_2 + 4e^- \rightarrow 2O^{2-} \qquad 1.4$$

These oxygen anions are incorporated into the cathode oxide lattice, and subsequently conducted across the electrolyte to the anode where they can undergo an oxidation reaction with a source of fuel to produce electrons. For SOFC, the fuel can be either H_2 or any hydrocarbon and the corresponding oxidation reactions are shown in Equations 1.5 and 1.6:

$$H_2 + O^{2-} \rightarrow H_2O + 2e^- \qquad 1.5$$

$$C_nH_{2n+2} + (3n+1)O^{2-} \rightarrow nCO_2 + (n+1)H_2O + 2(3n+1)e^- \qquad 1.6$$

MIEC electrodes are required on both sides of the electrolyte in the SOFC in order to provide electrons from an external circuit to react with gas phase O_2 at the cathode side and to remove electrons from the surface at the anode.

PREVIEW

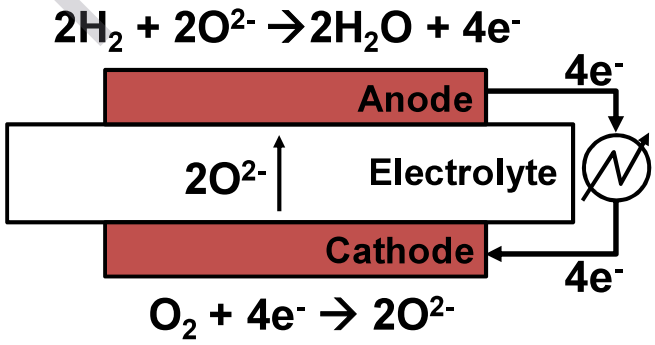


Figure 1.2: Operating principles for SOFC